IEEE Access
Multidisciplinary ⋮ Rapid Review ⋮ Open Access Journal

Received January 14, 2021, accepted January 17, 2021, date of publication January 19, 2021, date of current version January 27, 2021.

Digital Object Identifier 10.1109/ACCESS.2021.3052914

A Consequent-Pole Magnetic-Geared Machine With Axially Embedded Permanent Magnets for Hybrid Electric Vehicle

SHUANGCHUN XIE[1], (Graduate Student Member, IEEE), HAO CHEN[1], (Member, IEEE), YUEFEI ZUO[1], (Member, IEEE), FAWEN SHEN[1], (Graduate Student Member, IEEE), BOON SIEW HAN[2], CHI CUONG HOANG[2], AND CHRISTOPHER H. T. LEE[1], (Senior Member, IEEE)

[1]School of Electrical and Electronic Engineering, Nanyang Technological University, Singapore 639798
[2]Schaeffler Hub for Advanced Research at NTU (SHARE at NTU), Schaeffler (Singapore) Pte. Ltd., Singapore 539775

Corresponding author: Christopher H. T. Lee (chtlee@ntu.edu.sg)

This work was supported by the Schaeffler Group Research Grant M4062765.040.601001.

ABSTRACT This paper reveals the fundamental reason for the asymmetrical issue in magnetic-geared machines (MGMs) based on flux modulation theory. The analysis indicates that the magnetic circuits of three-phase windings in MGMs are inherently asymmetrical. This asymmetrical issue is even more severe in conventional consequent-pole MGMs (CP-MGMs) because of the more distorted magnetic field. Hence, to address the asymmetrical issue, a novel structure featuring enhanced harmonic elimination capability is proposed in this paper. Consequently, torque density can also be improved. In particular, the proposed CP-MGM employs modular structure and axially embedded permanent magnets (PMs) to achieve symmetrical back electromotive force (EMF) waveforms and improved torque capability, respectively. To further improve the electromagnetic performance of the proposed CP-MGM, the PM arc ratio and flux modulator width ratio are analytically designed, which provides a general design guideline for CP-MGMs. To illustrate the merits of the proposed CP-MGM, a few other MGMs are included for a fair comparison based on finite element analysis (FEA). Results show the proposed CP-MGM can achieve more symmetrical back EMF waveforms and lower torque ripple, as well as lower PM consumption and higher torque density, as compared with its MGM counterparts.

INDEX TERMS Asymmetrical magnetic circuit, cost-effective, high torque density, magnetic-geared machine.

I. INTRODUCTION

With increasing concerns about environmental pollution and energy crisis, hybrid electric vehicles (HEVs) have been attracting worldwide attention [1]. In particular, the series-parallel HEVs, including the most popular Toyota Prius, have dominated the market [2], [3]. Prius employs the mechanical planetary gear unit to decouple the speeds of the internal combustion engine (ICE) and the wheels, hence achieving optimal energy conversion under different driving conditions. However, the existence of mechanical gear would inevitably bring along noise, vibration, and abrasion. Hence, various electrical solutions, such as four-quadrant transducer, electric variable transmission, and dual mechanical-port electrical machine, were proposed to address the problems [4]–[7]. However, these electrical counterparts involve brushes and slip rings, hence resulting in low reliability and high maintenance cost.

To eliminate the brushes and slip rings, various magnetic-geared machines (MGMs) have been proposed [8]–[11]. These MGMs artfully integrates a flux-modulated magnetic gear [12] and a regular permanent magnet (PM) machine. It was shown that MGM is equivalent to a planetary gear combined with an electrical generator, therefore making it particularly suitable for constructing the power split device in HEV applications [13].

The associate editor coordinating the review of this manuscript and approving it for publication was Qinfen Lu.

Owing to its special operating principle, i.e., magnetic gearing effect, as well as dual mechanical-port structure, the performance characteristics of MGMs are quite different from that of conventional permanent magnet synchronous machines (PMSMs) [14]. Thus, the pole-pair combinations [15], [16], winding configurations [17], back electromotive force (EMF) harmonic characteristics [18], wide speed range operation [19], [20], and performance characteristics during overload conditions [21] have been investigated. In order to further improve the compactness and torque density of MGMs, the bidirectional flux-modulation effect, which integrates two flux modulation groups into one machine, was introduced [22]. Moreover, besides radial-flux MGMs, the corresponding axial-flux and transverse-flux counterparts were proposed [23]–[25]. These candidates could potentially achieve higher torque density, lower rotor losses, and higher efficiency than the radial-flux counterparts.

Existing MGMs utilize massive high-cost rare-earth PMs, which is one of the main obstacles for their industrial applications. Consequently, the consequent-pole MGMs (CP-MGMs) show promising potential for commercial applications as it can effectively reduce PM consumption. Nevertheless, the magnetomotive force (MMF) distribution of the consequent-pole structure is more distorted, i.e., there are even order harmonics [26]. On the other hand, it has been shown that the magnetic circuits of three-phase windings are asymmetrical in MGMs [10], [27]. As a result, the CP-MGMs are also vulnerable to asymmetrical back EMF waveforms as well as severe torque ripple.

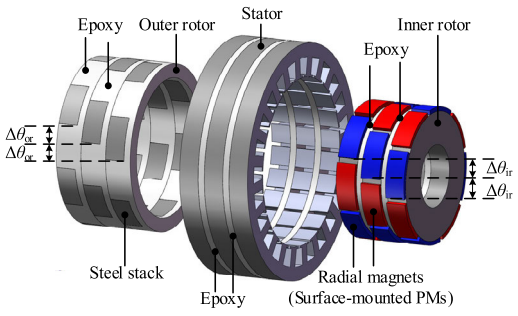

FIGURE 1. SM-MGM with complementary structure [27].

To address the asymmetrical magnetic circuit problem, a complementary structure was adopted in the surface-mounted MGM (SM-MGM) [27], as shown in Fig. 1. In this machine, both the inner rotor and outer rotor are divided into three modules to eliminate the most dominant magnetic field harmonic accounting for the asymmetry. However, the fundamental reason for the asymmetrical magnetic circuit is still unclear. Furthermore, the performance is not sufficiently satisfactory when this complementary structure is adopted in the CP-MGM, owing to the more distorted magnetic field distribution caused by the consequent-pole structure.

In this paper, the fundamental reason for the asymmetrical magnetic circuit is revealed by the flux modulation theory. Based on the analysis, a novel CP-MGM, which exhibits the advantage of enhanced harmonic elimination, i.e., the majority of the magnetic field harmonics can be eliminated, is proposed. Meanwhile, low PM consumption and high torque density can be achieved simultaneously by the proposed consequent-pole structure with axially embedded PMs. The performances of the proposed machine are further verified based on finite element analysis (FEA). To have a better illustration of the proposed CP-MGM, the existing complementary SM-MGM and CP-MGM are purposely included for a fair comparison.

II. ASYMMETRICAL MAGNETIC CIRCUITPHENOMENON IN MGMs

A. OPERATION PRINCIPLE OF MGMs

With the advantages of high-torque transmission capability, reduced vibration and noise, and inherent overload protection, magnetic gear (MG) has attracted much attention [28]–[30] since it was first proposed in 2001 [12]. By replacing the high-speed PM rotor in a MG with the stator winding, a corresponding MGM is generated.

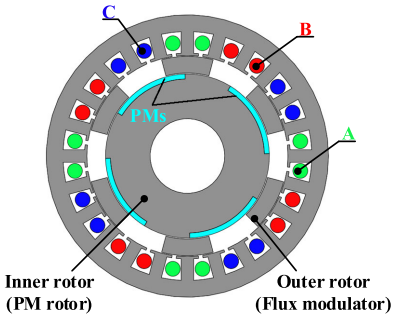

FIGURE 2. Cross section of the conventional CP-MGM.

Fig. 2 shows the cross section of a conventional CP-MGM, which comprises a 4 pole-pair inner PM rotor, a flux modulator, and a 24-slot stator. The flux modulator consists of 6 evenly distributed magnetic steel segments, while the stator consists of steel laminations and a 2 pole-pair single-layer distributed winding. By flux modulation theory [31], the 4 pole-pair magnetic field excited by the inner PM rotor is modulated by the flux modulator to generate a 2 pole-pair magnetic field, which interacts with the armature field to generate a steady electromagnetic torque. To get the highest transmitted torque, the pole-pair numbers of PM rotor (inner rotor), flux modulator (outer rotor), and stator windings are governed by

$$p_{or} = p_{ir} + p_s \tag{1}$$

where p_{ir}, p_{or}, and p_s are the pole-pair numbers of the inner rotor, outer rotor, and stator winding, respectively.

The speed and torque relationships of the stator winding, inner rotor, and outer rotor are

$$p_{ir} \times \omega_{ir} = p_{or} \times \omega_{or} - p_s \times \omega_s \tag{2}$$

$$T_{ir} = -\frac{p_{ir}}{p_{or}} T_{or} = \frac{p_{ir}}{p_s} T_s \tag{3}$$

where ω_{ir}, ω_{or}, and ω_s are the rotating speeds of the inner rotor, outer rotor, and stator winding, respectively. T_{ir}, T_{or}, and T_s are the torques of the inner rotor, outer rotor, and stator winding, respectively.

When the outer and inner rotors of an MGM are connected to the ICE crankshaft and wheels of an HEV, respectively, the speeds of ICE and wheels are decoupled by the stator winding. Hence, the power from ICE is transmitted to the wheels as traction power and transformed to the stator winding as electrical power. However, it is noted that the torque-transmitting relations of the two rotors are constant governed by the gear ratio. Therefore, a torque-regulating machine is required to decouple the ICE and the wheel torque. The MGM and torque-regulating machine constitute an electronic continuously variable transmission (eCVT), which can realize decouple control of the speed and torque of the ICE and wheels. From the above analysis, it can be seen that the MGM can realize the same function as the power split machine, making it particularly suitable for HEV applications.

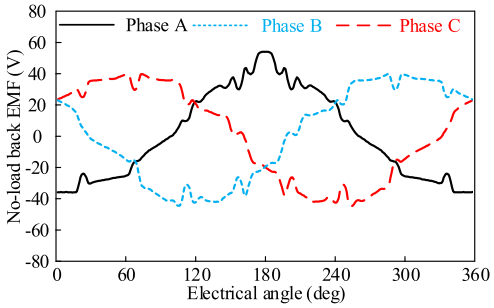

FIGURE 3. Back EMF waveforms of the conventional CP-MGM when the outer rotor rotates at 1600 r/min and the inner rotor rotates at 1200 r/min.

B. ASYMMETRICAL MAGNETIC CIRCUIT PHENOMENON

It has been found that in MGMs, the magnetic circuits of three-phase windings are asymmetrical [10], [27], hence resulting in asymmetrical back EMF waveforms. Taking the CP-MGM shown in Fig. 2 as an example, when both the inner rotor and outer rotor rotate at rated speeds, the no-load back EMF waveforms are shown in Fig. 3. As can be seen, the back EMF is non-sinusoidal and asymmetrical, which may result in severe torque ripple. In addition, the cogging torque is also significant. As shown in Fig. 4, the cogging torque is about 13.84 Nm (peak-peak value). This cogging torque is even larger than the rated torque that is about 10 Nm.

C. THEORETICAL ANALYSIS OF THE ASYMMETRICAL MAGNETIC CIRCUIT PHENOMENON

As mentioned in [27], the asymmetrical magnetic circuit phenomenon in MGMs should be attributed to some high-order harmonics. However, the fundamental reason is still unclear. Hence, this part contributes to revealing the essential reason for the asymmetrical phenomenon based on the analysis of back EMF harmonic characteristics.

In the CP-MGM, the MMF, F_{PM}, produced by inner rotor PMs and the airgap permeance, λ_f, can be

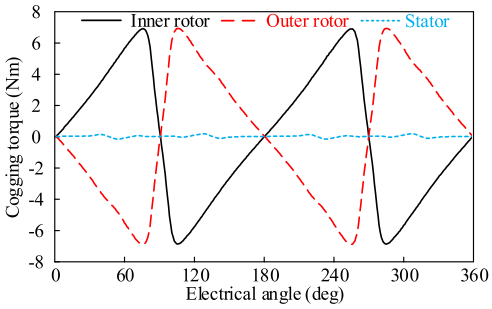

FIGURE 4. Cogging torque of conventional CP-MGM when the outer rotor rotates with the inner rotor latched.

expressed as

$$F_{PM}(\theta, t) = \sum_{n=1,2,3\ldots} F_n \cos(np_{ir}\theta - np_{ir}\omega_{ir}t) \tag{4}$$

$$\lambda_f(\theta, t) = \lambda_0 + \sum_{m=1,2,3\ldots} \lambda_m \cos(mp_{or}\theta - mp_{or}\omega_{or}t) \tag{5}$$

where θ and t are the spatial position and time, respectively; while F_n, λ_0, and λ_m are the amplitudes of n^{th} PM MMF, constant permeance part, and m^{th} permeance harmonic, respectively.

Hence, the flux density excited by PMs in the outer airgap can be derived by the flux modulation theory as

$$\begin{aligned} &B(\theta, t) \\ &= \sum_{n=1,2,3\ldots} F_n\lambda_0 \cos(np_{ir}\theta - np_{ir}\omega_{ir}t) \\ &\quad + \sum_{n=1,2,3\ldots} \sum_{m=1,2,3\ldots} \frac{F_n\lambda_m}{2} \\ &\quad \times \left\{ \begin{array}{l} \cos\left[(np_{ir} + mp_{or})\theta - (np_{ir}\omega_{ir} + mp_{or}\omega_{or})t\right] \\ + \cos\left[(np_{ir} - mp_{or})\theta - (np_{ir}\omega_{ir} - mp_{or}\omega_{or})t\right] \end{array} \right\} \end{aligned} \tag{6}$$

Here, the term $B_{n,m}$ is used to denote the magnetic field produced by n^{th} MMF and m^{th} permeance harmonics. It should be noticed that m can be negative and 0. More specifically, when $m = 0$, this harmonic is produced through the constant permeance part. Meanwhile, if m is negative, the corresponding pole-pair number is $np_{ir} - |m|p_{or}$. By flux modulation theory, the $(p_{or} - p_{ir})$-pole-pair magnetic field is the working harmonic, i.e., the working harmonic is denoted as $B_{1,-1}$.

To expediently derive the back EMF expression, the winding function theory is adopted as

$$\left\{ \begin{array}{l} N_a(\theta) = \sum_{j=1,3,5\ldots} N_j \cos(jp_s\theta) \\ N_b(\theta) = \sum_{j=1,3,5\ldots} N_j \cos(jp_s\theta - j\frac{2}{3}\pi) \\ N_c(\theta) = \sum_{j=1,3,5\ldots} N_j \cos(jp_s\theta + j\frac{2}{3}\pi) \\ N_j = \frac{2}{j\pi}\frac{N_s}{p_s}k_{wj} \end{array} \right. \tag{7}$$

where N_j is the amplitude of j^{th} harmonic of the armature winding function, N_s is the number of turns in series per phase, and k_{wj} is the corresponding winding factor.

Then, the back EMF of the CP-MGM is calculated by

$$e_x = -\frac{d}{dt}[r_g l_a \int_0^{2\pi} B(\theta, t) N_x(\theta) d\theta], \quad x = a, b, c \tag{8}$$

where r_g and l_a are the airgap radius and stack length, respectively.

Substituting (6) and (7) into (8), the back EMF can be expressed as

$$\begin{cases} e_a = \sum_{n=1,2,3\ldots} \sum_{m=0,\pm1,\pm2\ldots} E_{n,m} \\ \quad \times \sin[v'_{n,m}(p_{or}\omega_{or} - p_{ir}\omega_{ir})t] \\ e_b = \sum_{n=1,2,3\ldots} \sum_{m=0,\pm1,\pm2\ldots} E_{n,m} \\ \quad \times \sin[v'_{n,m}(p_{or}\omega_{or} - p_{ir}\omega_{ir})t - p'_{n,m}\frac{2}{3}\pi] \\ e_c = \sum_{n=1,2,3\ldots} \sum_{m=0,\pm1,\pm2\ldots} E_{n,m} \\ \quad \times \sin[v'_{n,m}(p_{or}\omega_{or} - p_{ir}\omega_{ir})t + p'_{n,m}\frac{2}{3}\pi] \end{cases} \tag{9}$$

$$E_{n,m} = \begin{cases} \pi F_n \lambda_0 r_g l_a n p_{ir}\omega_{ir} N_{p'_{n,m}}, & m = 0 \\ \pi F_n \frac{\lambda_m}{2} r_g l_a (n p_{ir}\omega_{ir} + m p_{or}\omega_{or}) N_{p'_{n,m}}, & m = \pm1, \pm2\ldots \end{cases} \tag{10}$$

$$p'_{n,m} = \frac{n p_{ir} + m p_{or}}{p_{or} - p_{ir}} \tag{11}$$

$$v'_{n,m} = \frac{n p_{ir}\omega_{ir} + m p_{or}\omega_{or}}{p_{or}\omega_{or} - p_{ir}\omega_{ir}} \tag{12}$$

where $E_{n,m}$ is the amplitude of the back EMF harmonic $e_{n,m}$ which is induced by the magnetic field $B_{n,m}$, $p'_{n,m}$ is the relative spatial order defined as the ratio of the pole-pair number of the magnetic field harmonic $B_{n,m}$ to that of the working harmonic $B_{1,-1}$, $v'_{n,m}$ is the relative frequency order defined as the ratio of the frequency of back EMF harmonic $e_{n,m}$ to that of the working component $e_{1,-1}$.

According to (9), (11), and (12), it can be seen that for specific back EMF harmonic $e_{n,m}$, the phase angle difference between the three phases is

$$\begin{aligned} \Delta\theta_{n,m} &= \frac{p'_{n,m}}{v'_{n,m}} \times \frac{2}{3}\pi \\ &= \frac{p_{or}\omega_{or} - p_{ir}\omega_{ir}}{p_{or} - p_{ir}} \Big/ \frac{n p_{ir}\omega_{ir} + m p_{or}\omega_{or}}{n p_{ir} + m p_{or}} \times \frac{2}{3}\pi \\ &= \frac{\omega_{1,-1}}{\omega_{n,m}} \times \frac{2}{3}\pi = \frac{1}{\omega'_{n,m}} \times \frac{2}{3}\pi \end{aligned} \tag{13}$$

where $\omega_{1,-1}$ and $\omega_{n,m}$ are the mechanical speed of the working harmonic $B_{1,-1}$ and magnetic field harmonic $B_{n,m}$, respectively; while $\omega'_{n,m}$ is the harmonic relative speed defined as the ratio of $\omega_{n,m}$ to $\omega_{1,-1}$.

As can be seen, for different back EMF harmonics $e_{n,m}$, the phase angle differences among the three phases are not necessarily the same as 120 degrees, instead, they are dependent on the rotating speeds of magnetic field harmonics. Fig. 5 shows the rotating speeds of magnetic field harmonics in the CP-MGM, indicating that magnetic field harmonics may rotate at different speeds, owing to the special working principle, i.e., magnetic gearing effect, and dual mechanical-port structure. Consequently, according to (13), for fundamental back EMF component $e_{1,-1}$, the phase angle differences among the three phases are 120 degrees. However, for other back EMF harmonics $e_{n,m}$, the phase angle differences among the three phases are different. As a result, the back EMF waveforms are asymmetrical for the three-phase windings. In conclusion, the asymmetrical magnetic circuit problem is a common issue for MGMs, which should be attributed to the magnetic gearing effect and dual mechanical-port structure.

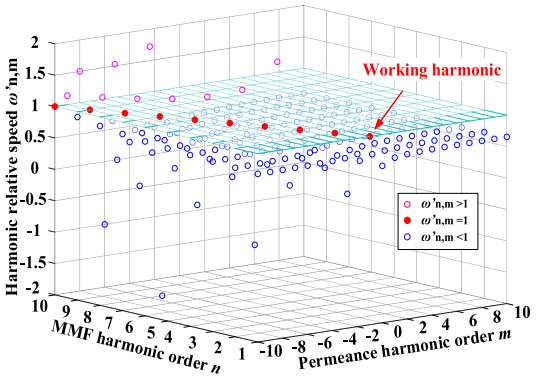

FIGURE 5. Relative speeds of magnetic field harmonics in the CP-MGM.

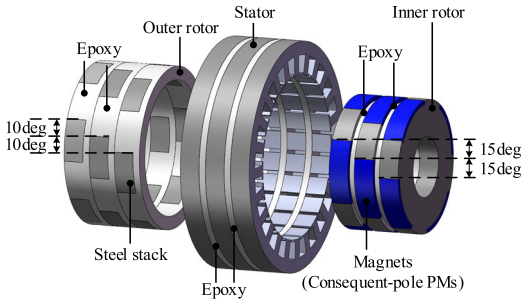

FIGURE 6. CP-MGM with existing complementary structure.

III. PRINCIPLE AND CHARACTERISTICS OF THE PROPOSED STRUCTURE

It was revealed in section II that the asymmetrical magnetic circuit problem is a common issue for MGMs. Moreover, this asymmetrical issue is more severe in CP-MGMs because of the further distorted magnetic field. Consequently, the performance is not sufficiently satisfactory when the existing complementary structure is adopted in the CP-MGM, as shown in Fig. 6. Therefore, a novel CP-MGM with axially embedded PMs is proposed in this paper, as shown in Fig. 7. Compared with the complementary structure, the proposed

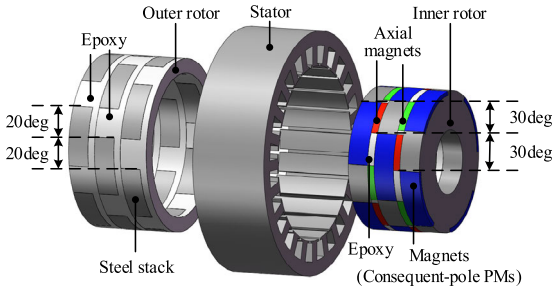

FIGURE 7. Proposed CP-MGM with axially embedded PMs.

CP-MGM employs the artfully designed axially shifted angles ($\Delta\theta_{ir}$ and $\Delta\theta_{or}$) and axially embedded PMs. As a result, it can exhibit the absolute advantages of enhanced harmonic elimination and improved torque capability.

A. ENHANCED HARMONIC ELIMINATION

As shown in Fig. 7, the novel structure can also be considered as a combination of three modules having different initial rotor positions. Hence, the working harmonic of the y^{th} module ($y = 1$, 2, or 3) can be calculated as

$$B_{1,-1,y} = \frac{F_1\lambda_1}{2}\cos\begin{bmatrix}(p_{ir}-p_{or})\theta-(p_{ir}\omega_{ir}-p_{or}\omega_{or})t\\+(y-1)(p_{ir}\Delta\theta_{ir}-p_{or}\Delta\theta_{or})\end{bmatrix} \tag{14}$$

where $\Delta\theta_{ir}$ and $\Delta\theta_{or}$ are the axially shifted angles among adjacent modules of the inner rotor and outer rotor, respectively. Therefore, the working harmonics of the three modules are identical and the output torque could be maintained if the axially shifted angles comply with

$$p_{or}\Delta\theta_{or} = p_{ir}\Delta\theta_{ir} \tag{15}$$

Furthermore, the magnetic field harmonic $B_{n,m}$ of the y^{th} ($y = 1$, 2, or 3) module can be expressed as

$$B_{n,m,y} = \frac{F_n\lambda_m}{2}\cos\begin{bmatrix}(np_{ir}+mp_{or})\theta-(np_{ir}\omega_{ir}+mp_{or}\omega_{or})t\\+(y-1)(np_{ir}\Delta\theta_{ir}+mp_{or}\Delta\theta_{or})\end{bmatrix} \tag{16}$$

By carefully designing axially shifted angles $\Delta\theta_{ir}$ and $\Delta\theta_{or}$, the following relationship can be achieved

$$B_{n,m,1} + B_{n,m,2} + B_{n,m,3} = 0 \tag{17}$$

According to (16) and (17), the magnetic field harmonic $B_{n,m}$ is eliminated, under the condition of

$$np_{ir}\Delta\theta_{ir} + mp_{or}\Delta\theta_{or} = l\frac{2}{3}\pi \tag{18}$$

where l is an integer that is not a multiple of 3. In the proposed structure, the axially shifted angles of the inner rotor and outer rotor are designed as

$$p_{or}\Delta\theta_{or} = p_{ir}\Delta\theta_{ir} = \frac{2}{3}\pi \tag{19}$$

It should be noted that both the inner rotor and outer rotor are shifted by 120 electrical degrees. As a result, the harmonic $B_{n,m}$ can be eliminated when $(n + m)$ is not a multiple of 3. In other words, all the harmonics are eliminated if the constituting MMF order n and permeance order m comply with

$$n + m \neq 3q, \quad q = 0, \pm1, \pm2, \ldots \tag{20}$$

To conclude, the enhanced harmonic elimination effect is realized in the proposed structure by the axially shifted angles given by (19). By contrast, the existing complementary structure was designed to eliminate the most dominant magnetic field harmonic accounting for the asymmetrical phenomenon, which is $B_{1,-3}$ in terms of the investigated CP-MGM [27]. Thus, following the method presented in [27], both the inner rotor and outer rotor are shifted by 60 electrical degrees, as shown in Fig. 6.

TABLE 1. Harmonic elimination effect of the complementary and proposed structures.

Pole-pair number	2	2	4	4	6	8	8	14
MMF order n	1	2	1	2	3	1	2	1
Permeance order m	-1	-1	0	-2	-1	-2	0	-3
Complementary MGM	×	×	×	×	√	×	√	√
Proposed MGM	×	√	√	×	√	√	√	√

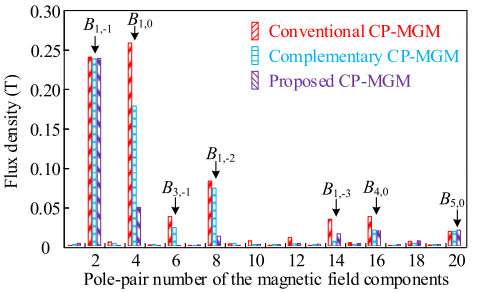

FIGURE 8. Comparison of the magnetic field distribution in CP-MGMs with different structures.

Table 1 compares the harmonic elimination effect of the existing complementary structure and the proposed structure, where "√" indicates the specific harmonic is eliminated in the corresponding structure, while "×" means the opposite. It can be seen that the majority of non-working harmonics are eliminated by the proposed structure as compared with the existing complementary structure. Fig. 8 shows the flux density distribution of three CP-MGMs, namely, the conventional CP-MGM, the CP-MGM equipped with the complementary structure, and the proposed CP-MGM. As can be seen, both the complementary and proposed structures can maintain the working harmonic $B_{1,-1}$, as well as eliminate the non-working harmonics. Moreover, it implies the major distinction of the proposed structure comes from the absolute advantage of enhanced harmonic elimination.

To verify the above analysis, Fig. 9 compares the back EMF waveforms of the CP-MGMs with the complementary and

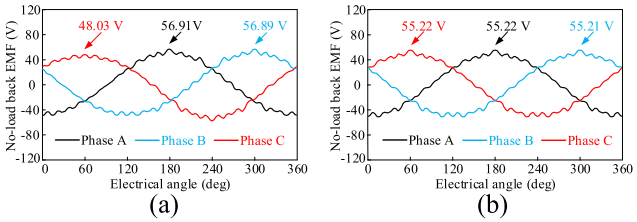

FIGURE 9. Back EMF waveforms of CP-MGMs when the outer and inner rotors rotate at 1600 r/min and 1200 r/min, respectively. (a) With complementary structure. (b) With proposed structure.

proposed structures. As can be seen, the asymmetrical phenomenon can be significantly alleviated by both structures, when compared with the conventional CP-MGM as shown in Fig.3. However, there still exists noticeable asymmetry in the complementary CP-MGM, which can only be eliminated by the proposed structure.

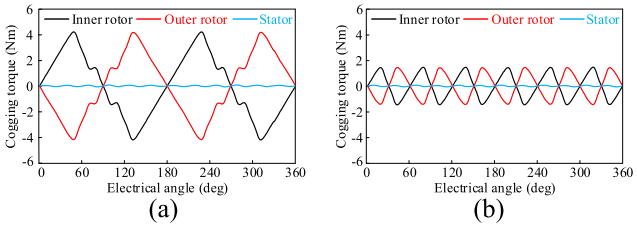

FIGURE 10. Cogging torque waveforms of CP-MGMs (the inner rotor is latched but the outer rotor rotates). (a) With complementary structure. (b) With proposed structure.

Furthermore, the cogging torque waveforms are shown in Fig. 10. Compared with that of the conventional CP-MGM as shown in Fig. 4, the peak-peak cogging torques are reduced from 13.84 Nm to 8.5 Nm and 2.96 Nm, by employing the complementary and proposed structures, respectively. Hence, the conclusion can be drawn that the proposed structure outperforms the complementary structure by the advantage of enhanced harmonic elimination. To improve the readability of this paper, as the worst performing candidate, the conventional CP-MGM will be omitted in the following sections.

B. ENHANCED TORQUE DENSITY BY AXIALLY EMBEDDED PMS

In the complementary structure, the epoxy-made flux barrier is indispensable for reducing axial flux leakage among adjacent modules. However, the torque density would inevitably get reduced because of the reduced effective stack length. To improve the situation, the axial magnetized PMs are embedded in the flux barrier of inner rotor to concentrate the flux and enhance airgap flux density in the proposed structure, as shown in Fig. 11. Consequently, the output torque can be improved.

It should be noted that the flux barrier width also affects the output torque. More specifically, a thicker flux barrier contributes to reducing axial flux leakage, which results in increased airgap flux density and output torque. On the other hand, the thicker flux barrier also results in reduced effective stack length. Therefore, there exists an optimal flux barrier width to maximize the output torque and torque density. To take into account the manufacturing complexity and facilitate a fair comparison, the flux barrier width in the proposed structure is set as 5 mm, which is the same value used in the existing complementary SM-MGM [27].

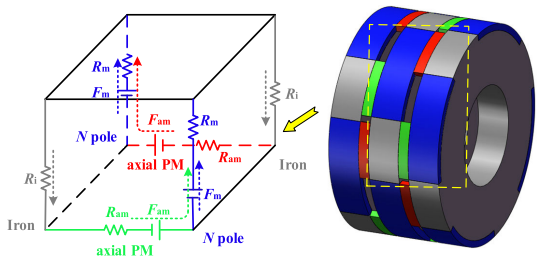

FIGURE 11. Simplified magnetic circuits of the axially embedded PMs. F_m and R_m are the MMF and reluctance of the radial magnetized PMs, F_{am} and R_{am} are the MMF and reluctance of the axially embedded PMs, and R_i is the reluctance of the iron pole.

According to Fig. 11, the axially magnetized PMs should be embedded between the consequent-pole PMs and iron poles. Thus, the axially embedded PM arc ratio β_{PM} is designed as

$$\beta_{PM} = \min\{\alpha_{PM}, 1-\alpha_{PM}, \Delta\alpha_{ir}\} \tag{21}$$

where α_{PM} is the consequent-pole PM arc ratio, and $\Delta\alpha_{ir}$ is related to the axially shifted angle, defined as $\Delta\alpha_{ir} = p_{ir}\Delta\theta_{ir}/(2\pi)$. Moreover, to provide flux path for the axially embedded PMs, the flux barrier in the stator is substituted by the iron core, as shown in Fig. 7.

IV. OPTIMIZATION OF THE PROPOSED CP-MGM

With the advantage of enhanced harmonic elimination, the majority of the non-working magnetic field harmonics are eliminated by the proposed structure. However, the rest of the non-working harmonics still result in cogging torque and back EMF harmonics. On the other hand, although torque density is improved by the axially embedded PMs, the PM utilization ratio is deteriorated because of the severe magnetic saturation. Therefore, the proposed CP-MGM is further optimized in terms of cogging torque, back EMF, and PM utilization ratio.

A. OPTIMIZATION OF COGGING TORQUE

As shown in Fig. 10 (b), the cogging torque of the inner rotor and outer rotor have the same amplitude but opposite directions, indicating the cogging torque is mainly generated by the interaction of the two rotors. Thus, to simplify the analysis, the outer rotor is kept stationary while the inner rotor rotates. Based on Maxwell's stress tensor, the cogging torque is calculated as

$$T_c(\alpha) = \frac{1}{\mu_0} l_a r^2 \int_0^{2\pi} B_{sr}(r,\theta,\alpha) B_{s\theta}(r,\theta,\alpha) d\theta \tag{22}$$

where μ_0 is the permeability of vacuum, r is the radius of the integration surface, and α is the inner rotor position. B_{sr} and $B_{s\theta}$ are the radial and tangential flux density components at radius r, respectively.

The radial and tangential components of the flux density in the inner airgap is derived from the flux modulation effect as

$$\begin{aligned}
&B_{sr}(r,\theta,\alpha)\\
&=B_r(r,\theta,\alpha)\lambda_a(r,\theta)+B_\theta(r,\theta,\alpha)\lambda_b(r,\theta)\\
&=\lambda_0(r)\sum\nolimits_n B_{rn}\cos[np_{ir}(\theta-\alpha)]\\
&\quad+\sum\nolimits_m\sum\nolimits_n B_{rn}(r)\lambda_{am}(r)\cos[np_{ir}(\theta-\alpha)]\cos(mp_{or}\theta)\\
&\quad+\sum\nolimits_m\sum\nolimits_n B_{\theta n}(r)\lambda_{bm}(r)\sin[np_{ir}(\theta-\alpha)]\sin(mp_{or}\theta)\\
&B_{s\theta}(r,\theta,\alpha)\\
&=B_\theta(r,\theta,\alpha)\lambda_a(r,\theta)-B_r(r,\theta,\alpha)\lambda_b(r,\theta)\\
&=\lambda_0(r)\sum\nolimits_n B_{\theta n}\cos[np_{ir}(\theta-\alpha)]\\
&\quad+\sum\nolimits_m\sum\nolimits_n B_{\theta n}(r)\lambda_{am}(r)\sin[np_{ir}(\theta-\alpha)]\cos(mp_{or}\theta)\\
&\quad-\sum\nolimits_m\sum\nolimits_n B_{rn}(r)\lambda_{bm}(r)\cos[np_{ir}(\theta-\alpha)]\sin(mp_{or}\theta)
\end{aligned}\tag{23,24}$$

where B_r and B_θ are the radial and tangential flux density components in the slotless inner airgap, respectively; λ_a and λ_b are the real and imaginary parts of the complex relative airgap permeance, respectively.

Thus, the cogging torque expression is calculated as expressed in (25). The integrals in (25) will yield a result different from zero only for certain n, k, m, and h. Here, the second term of (25) is taken as an example, which is rewritten as (26), as shown at the bottom of the next page.

It is easy to show that when

$$kp_{ir}+np_{ir}-hp_{or}=0 \tag{27}$$

where k, n, and h are the orders of radial and tangential magnetic field harmonics, and the real part of the relative permeance harmonics, respectively. The cogging torque is

$$T_c(\alpha)=-\frac{\pi}{2}\frac{1}{\mu_0}l_a r^2\lambda_0\sum_n\sum_k\sum_h B_{rn}B_{\theta k}\lambda_{ah}\sin[(k+n)p_{ir}\alpha] \tag{28}$$

Similarly, when

$$kp_{ir}-np_{ir}+hp_{or}=0 \text{ or } kp_{ir}-np_{ir}-hp_{or}=0 \tag{29}$$

the corresponding cogging torque is

$$T_c(\alpha)=-\frac{\pi}{2}\frac{1}{\mu_0}l_a r^2\lambda_0\sum_n\sum_k\sum_h B_{rn}B_{\theta k}\lambda_{ah}\sin[(k-n)p_{ir}\alpha] \tag{30}$$

$$\begin{aligned}
T_c(\alpha)=\frac{1}{\mu_0}l_a r^2\Bigg\{&\lambda_0^2\sum_n\sum_k B_{rn}B_{\theta k}\int_0^{2\pi}\cos[np_{ir}(\theta-\alpha)]\sin[np_{ir}(\theta-\alpha)]d\theta\\
&+\lambda_0\sum_n\sum_k\sum_h B_{rn}B_{\theta k}\lambda_{ah}\int_0^{2\pi}\cos[np_{ir}(\theta-\alpha)]\sin[kp_{ir}(\theta-\alpha)]\cos(hp_{or}\theta)d\theta\\
&-\lambda_0\sum_n\sum_k\sum_h B_{rn}B_{rk}\lambda_{bh}\int_0^{2\pi}\cos[np_{ir}(\theta-\alpha)]\cos[kp_{ir}(\theta-\alpha)]\sin(hp_{or}\theta)d\theta\\
&+\lambda_0\sum_n\sum_k\sum_m B_{rn}B_{\theta k}\lambda_{am}\int_0^{2\pi}\cos[np_{ir}(\theta-\alpha)]\sin[kp_{ir}(\theta-\alpha)]\cos(mp_{or}\theta)d\theta\\
&+\lambda_0\sum_n\sum_k\sum_m B_{\theta n}B_{\theta k}\lambda_{bm}\int_0^{2\pi}\sin[np_{ir}(\theta-\alpha)]\sin[kp_{ir}(\theta-\alpha)]\sin(mp_{or}\theta)d\theta\\
&+\sum_n\sum_k\sum_m\sum_h B_{rn}B_{\theta k}\lambda_{am}\lambda_{ah}\int_0^{2\pi}\cos[np_{ir}(\theta-\alpha)]\sin[kp_{ir}(\theta-\alpha)]\cos(mp_{or}\theta)\cos(hp_{or}\theta)d\theta\\
&+\sum_n\sum_k\sum_m\sum_h B_{\theta n}B_{\theta k}\lambda_{bm}\lambda_{ah}\int_0^{2\pi}\sin[np_{ir}(\theta-\alpha)]\sin[kp_{ir}(\theta-\alpha)]\sin(mp_{or}\theta)\cos(hp_{or}\theta)d\theta\\
&-\sum_n\sum_k\sum_m\sum_h B_{rn}B_{rk}\lambda_{am}\lambda_{bh}\int_0^{2\pi}\cos[np_{ir}(\theta-\alpha)]\cos[kp_{ir}(\theta-\alpha)]\cos(mp_{or}\theta)\sin(hp_{or}\theta)d\theta\\
&-\sum_n\sum_k\sum_m\sum_h B_{\theta n}B_{rk}\lambda_{bm}\lambda_{bh}\int_0^{2\pi}\sin[np_{ir}(\theta-\alpha)]\cos[kp_{ir}(\theta-\alpha)]\sin(mp_{or}\theta)\sin(hp_{or}\theta)d\theta\Bigg\}
\end{aligned}\tag{25}$$

TABLE 2. Combinations of n, k, and h that satisfies $kp_{ir} + np_{ir} - hp_{or} = 0$.

k	1	2	1	2	3	4	5	1	2	3	4	5	6
n	2	1	5	4	3	2	1	8	7	6	5	4	3
h	2	2	4	4	4	4	4	6	6	6	6	6	6
k+n-h	1	1	2	2	2	2	2	3	3	3	3	3	3
Eliminate	√	√	√	√	√	√	√	×	×	×	×	×	×

For all the other combinations of n, k, and h, the cogging torque is equal to zero. Moreover, the proposed structure also contributes to reducing the cogging torque. Specifically, taking the case of (27) as an example, the cogging torque of the other two modules $T_c2(\alpha)$ and $T_c3(\alpha)$ is expressed as

$$\begin{aligned} T_{c2}(\alpha) &= -\frac{\pi}{2}\frac{1}{\mu_0} l_a r^2 \lambda_0 \sum_n \sum_k \sum_h B_{rn} B_{\theta k} \lambda_{ah} \\ &\quad \times \sin[(k+n)p_{ir}(\alpha + \Delta\theta_{ir}) - hp_{or}\Delta\theta_{or}] \\ &= T_c[\alpha + (k+n-h)\frac{2}{3}\pi] \end{aligned} \tag{31}$$

$$\begin{aligned} T_{c3}(\alpha) &= -\frac{\pi}{2}\frac{1}{\mu_0} l_a r^2 \lambda_0 \sum_n \sum_k \sum_h B_{rn} B_{\theta k} \lambda_{ah} \\ &\quad \times \sin[(k+n)p_{ir}(\alpha + 2\Delta\theta_{ir}) - 2hp_{or}\Delta\theta_{or}] \\ &= T_c[\alpha + (k+n-h)\frac{4}{3}\pi] \end{aligned} \tag{32}$$

Consequently, the combined cogging torque $T_c^*(\alpha)$ is

$$\begin{aligned} T_c^*(\alpha) = T_c(\alpha) &+ T_c[\alpha + (k+n-h)\frac{2}{3}\pi] \\ &+ T_c[\alpha + (k+n-h)\frac{4}{3}\pi] \end{aligned} \tag{33}$$

Thus, it can be found that the combined cogging torque is eliminated by the proposed structure, except when

$$k + n - h = 3i, \quad i = 0, \pm 1, \ \pm 2, \ldots \tag{34}$$

Neglecting high-order harmonics, the combinations of k, n, and h that meet the condition of $kp_{ir} + np_{ir} - hp_{or} = 0$ are listed in Table 2. As highlighted, the 6th relative permeance harmonic interacts with multiple magnetic field harmonics, such as 1st, 2nd, 3rd, 4th, 5th, 6th, 7th, and 8th, to generate cogging torque, while they cannot be eliminated by the proposed modular structure. It is challenging to eliminate multiple flux density harmonics simultaneously, especially the 1st magnetic field component also contributes to average torque. Therefore, the 6th relative permeance harmonic should be eliminated to reduce the cogging torque. Likewise, when (29) holds or consider other terms of (25), the same conclusion can be drawn.

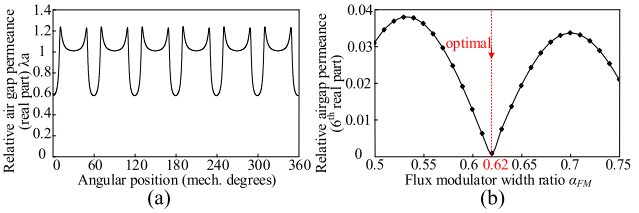

FIGURE 12. The relative airgap permeance obtained by conformal mapping. (a) The real part of the relative permeance when the flux modulator width ratio α_{FM} is 0.7. (b) The variation of the 6th real part relative permeance harmonic against flux modulator width ratio α_{FM}.

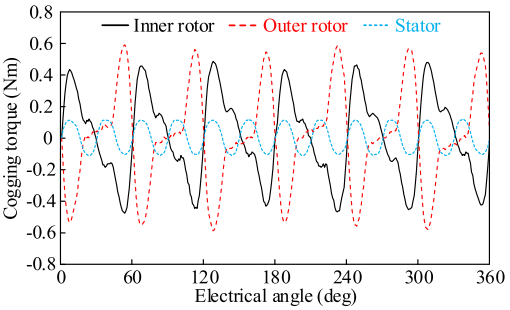

FIGURE 13. Cogging torque of the proposed CP-MGM with flux modulator width ratio α_{FM} as 0.62.

The complex relative airgap permeance is obtained by conformal mapping [32]. The calculated real part of the relative permeance λ_a is shown in Fig. 12(a), and the variation of the 6th real part relative permeance harmonic with flux modulator width ratio α_{FM} is shown in Fig. 12 (b). The analytical results indicate that the optimal α_{FM} for the investigated CP-MGM is 0.62, and the resultant cogging torque is shown in Fig. 13. As can be seen, the peak-peak cogging torque is effectively reduced from 2.96 Nm to 1.18 Nm, as compared with that shown in Fig. 10 (b). It should be noted that the optimal flux modulator width ratio α_{FM} is related to inner and outer rotor pole-pair numbers. Hence, the optimal α_{FM} derived in this paper, i.e., 0.62, may not apply to other MGMs with different pole-pair combinations, but the proposed design method in this paper can be easily extended to other MGMs.

$$\begin{aligned} T_c(\alpha) &= \frac{1}{\mu_0} l_a r^2 \lambda_0 \sum_n \sum_k \sum_h B_{rn} B_{\theta k} \lambda_{ah} \times \int_0^{2\pi} \cos[np_{ir}(\theta - \alpha)] \sin[kp_{ir}(\theta - \alpha)] \cos(hp_{or}\theta) d\theta \\ &= \frac{1}{\mu_0} l_a r^2 \lambda_0 \sum_n \sum_k \sum_h B_{rn} B_{\theta k} \lambda_{ah} \\ &\quad \times \frac{1}{4} \int_0^{2\pi} \left\{ \begin{aligned} &\sin[(kp_{ir} + np_{ir} + hp_{or})\theta - (kp_{ir} + np_{ir})\alpha] + \sin[(kp_{ir} + np_{ir} - hp_{or})\theta - (kp_{ir} + np_{ir})\alpha] \\ &+ \sin[(kp_{ir} - np_{ir} + hp_{or})\theta - (kp_{ir} - np_{ir})\alpha] + \sin[(kp_{ir} - np_{ir} - hp_{or})\theta - (kp_{ir} - np_{ir})\alpha] \end{aligned} \right\} d\theta \end{aligned} \tag{26}$$

TABLE 3. The dominant flux linkage components.

Flux linkage $\varphi_{n,m}$ (mWb)	100.3	11.58	3.59	2.89	1.70	1.08	0.82	0.37	0.32	0.27	0.23	0.22	0.17	0.16	0.15
MMF order n	1	2	4	0	5	1	1	8	3	1	2	3	7	6	1
Permeance order m	-1	-1	-3	1	-3	3	-3	-5	-3	1	1	-1	-5	-3	-9
$n+m$	0	1	1	1	2	4	-2	-3	0	2	3	2	2	3	8
Eliminate	×	√	√	√	√	√	√	×	×	√	×	√	√	×	√

B. OPTIMIZATION OF BACK EMF WAVEFORMS

When the CP-MGM operates as a power split machine, the speeds of the inner rotor and outer rotor are variable. Moreover, it was found that the amplitudes and orders of back EMF harmonics are variable with rotor speeds in MGMs [18]. Therefore, the most essential quantity to reflect back EMF harmonic is the flux linkage component. However, different flux linkage components may have the same frequency under certain operating conditions, owing to the dual mechanical-port structure. Thus, the flux linkage separation method presented in [18] is employed here to identify the specific flux linkage harmonics that lead to back EMF distortion.

The main flux linkage components are listed in Table 3, as shown at the bottom of next page. From the analysis in Section III-A, the flux linkage $\varphi_{n,m}$ is eliminated by the proposed structure if $(n + m)$ is not a multiple of 3. Thus, the dominant flux linkage components accounting for back EMF distortion are $\varphi_{8,-5}$, $\varphi_{3,-3}$, $\varphi_{2,1}$, and $\varphi_{6,-3}$, as highlighted in Table 3. The airgap permeance harmonic content is already optimized to reduce cogging torque. Hence, in this part, the consequent-pole PM arc ratio α_{PM} is optimized to eliminate the corresponding PM MMF harmonics. More specifically, the 2nd, 3rd, 6th, and 8th PM MMF harmonics should be minimized.

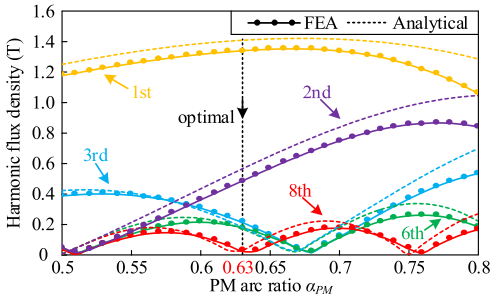

FIGURE 14. The variation of flux density harmonics of an equivalent slotless consequent-pole PM machine against its PM arc ratio α_{PM}.

The PM MMF harmonic content cannot be obtained straightforwardly by FEA. Hence, the corresponding flux density harmonics of an equivalent slotless consequent-pole PM machine, which are proportional to the MMF harmonics, are investigated instead. Fig. 14 shows the influences of PM arc ratio α_{PM} on the corresponding flux density harmonics, as derived by the analytical model and verified by FEA. To reduce the corresponding MMF harmonics that cause back EMF distortion and to maintain the output torque, the optimal α_{PM} is selected as 0.63. The optimal back EMF waveform is shown in Fig. 15. As can be seen, the back EMF harmonics are noticeably reduced as compared with that in Fig. 9 (b).

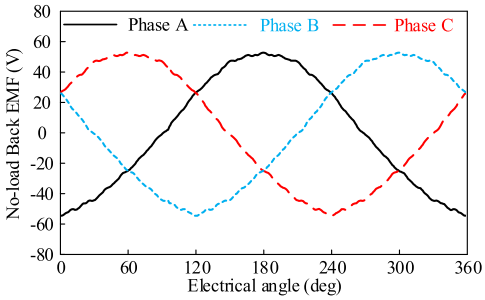

FIGURE 15. The back EMF waveforms of the proposed CP-MGM with the optimal PM arc ratio α_{PM}.

C. OPTIMIZATION OF PM UTILIZATION RATIO

Although the output torque is enhanced by the axially embedded PMs, the PM utilization ratio is reduced because of the severe magnetic saturation. Particularly, the saturation in the flux modulator should be mitigated as it impairs the flux modulation effect and hence torque capability.

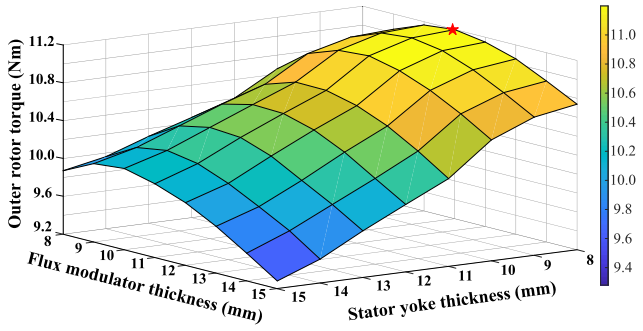

FIGURE 16. The variation of outer rotor torque against the thicknesses of flux modulator and stator yoke.

Therefore, 3D-FEA has been carried out to investigate the influence of the stator yoke and flux modulator thicknesses on torque capabilities, and the results are shown in Fig. 16. As can be seen, the optimal torque output can be obtained when the flux modulator and stator yoke thicknesses are 11 mm and 8 mm, respectively. More specifically, a torque improvement of 14.29% is achieved by employing 21.16% more PMs.

V. PERFORMANCE COMPARISONS AND ANALYSIS

To have a better demonstration of the proposed CP-MGM, performance comparisons of the existing complementary SM-MGM [27] (as shown in Fig. 1), the complementary

TABLE 4. Main parameters of the three MGMs.

Parameters	MGM1	MGM2	MGM3
Stator outer radius		85 mm	
Stator inner radius	60.6 mm	60.6 mm	62.6 mm
Width of stator teeth		6.8 mm	
Thickness of stator yoke	10 mm	10 mm	8 mm
Number of stator slot		24	
Outer rotor rated speed		1600 r/min	
Inner rotor rated speed		1200 r/min	
Pole-pairs of windings		2	
Pole-pairs of outer rotor		6	
Pole-pairs of inner rotor		4	
Thickness of flux modulator	10 mm	10 mm	11 mm
Flux modulator width ratio	0.5	0.5	0.62
Airgap length		0.6 mm	
PM thickness		3 mm	
PM arc ratio	0.9	0.7	0.63
Outer radius of inner rotor	49.4 mm	49.4 mm	50.4 mm
Inner radius of inner rotor		22 mm	
Stack length		55 mm	
Flux barrier width		5 mm	
Number of turns per slot		34	
Material of iron core		50JN1300	
Material of magnet		NdFeB (B_r=1.2T)	

MGM1: Complementary SM-MGM [27]; MGM2: Complementary CP-MGM; MGM3: The proposed CP-MGM.

TABLE 5. THD comparison of the three machines.

THD	Complementary SM-MGM	Complementary CP-MGM	Proposed CP-MGM
Phase A	4.85%	6.16%	2.90%
Phase B	4.89%	6.70%	2.90%
Phase C	4.89%	9.76%	2.87%

CP-MGM (as shown in Fig. 6), and the proposed CP-MGM (as shown in Fig. 7) are compared in terms of back EMF, torque characteristics, and PM utilization ratio. The results are obtained by 3D-FEA, while their main design parameters are shown in Table 4. It should be noted that the flux modulator thickness of the proposed CP-MGM is designed as 11 mm by taking into account the magnetic saturation caused by axial magnetized PMs, with details being presented in section IV.

A. BACK EMF

Fig. 17 shows the back EMF waveforms of the three machines and the corresponding harmonic spectrum, while the total harmonic distortion (THD) values are summarized in Table 5. As can be seen, the back EMF of the complementary CP-MGM is the most distorted, and there still exists significant asymmetry among three phases. This implies the performance is not satisfactory when the existing complementary structure is adopted in the CP-MGM, owing to the more distorted magnetic field distribution. Although the back EMF waveforms of the existing complementary SM-MGM are more sinusoidal and symmetrical, it exhibits the lowest fundamental back EMF with the maximum volume of PMs. In contrast, the proposed CP-MGM exhibits the most sinusoidal and symmetrical back EMF, as well as the highest

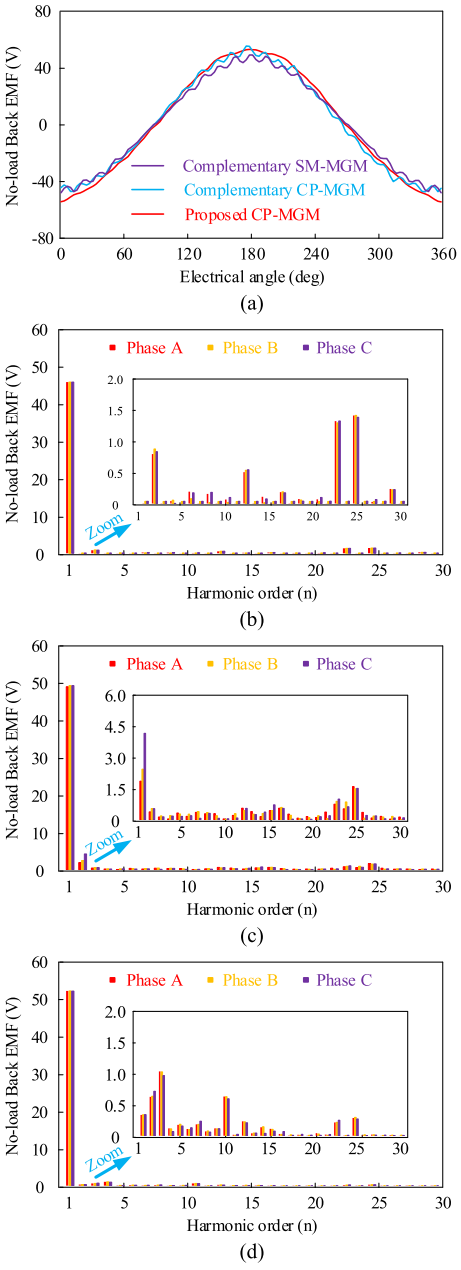

FIGURE 17. 3D-FEA predicted back EMF. (a) Back EMF waveforms of Phase A. (b) Harmonic spectrum of the complementary SM-MGM. (c) Harmonic spectrum of the complementary CP-MGM. (d) Harmonic spectrum the proposed CP-MGM.

fundamental back EMF, attributed to the proposed modular structure with axially embedded PMs.

B. TORQUE CHARACTERISTICS

As the reluctance torque is negligible in MGMs, $i_d = 0$ control is implemented to drive the machines at rated condition, i.e., the inner and outer rotors rotate at 1200 r/min and 1600 r/min, respectively, with the stator current of 8.5 A (rms). As a result, the electromagnetic torques of the three machines are compared in Fig. 18 and listed in Table 6.

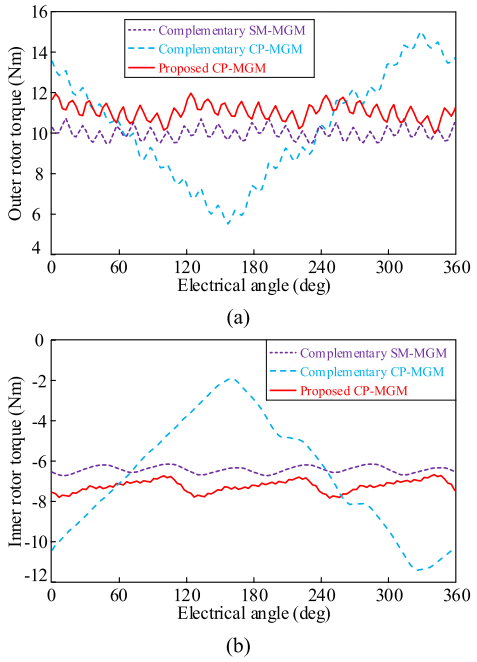

FIGURE 18. Output torque comparisons with $i_d = 0$ control. (a) Outer rotor torque. (b) Inner rotor torque.

TABLE 6. Torque comparisons of the three machines.

Items	Average torque (Nm)		Torque ripple (%)	
	Outer	Inner	Outer	Inner
Complementary SM-MGM	9.79	6.47	12.07	8.90
Complementary CP-MGM	10.21	6.75	79.24	126.81
Proposed CP-MGM	11.20	7.49	16.52	15.35

As can be seen, the complementary CP-MGM suffers from severe torque ripple, while the proposed CP-MGM obtains a significantly reduced torque ripple and enhanced torque density. Furthermore, as compared with the existing complementary SM-MGM, the proposed CP-MGM utilizes less PMs but increases its inner rotor torque and outer rotor torque by 15.8% and 14.4%, respectively.

TABLE 7. PM volume and PM utilization ratio of the three machines.

Items	Complementary SM-MGM	Complementary CP-MGM	Proposed CP-MGM
V_{m} (cm^3)	36.57	28.44	32.27
ε_m (Nm/cm^3)	0.27	0.36	0.35

C. PM UTILIZATION

Table 7 compares the PM consumption of the three machines, where PM utilization ratio ε_m is defined as the ratio of the outer rotor torque to PM volume V_{m}. As can be seen, the existing complementary SM-MGM exhibits the maximum PM volume and the lowest utilization ratio. On the other hand, the complementary CP-MGM utilizes the least volume of PMs and obtains the highest PM utilization ratio, attributed to the merits of consequent-pole structure. However, it suffers from serious torque ripple. In contrast, the proposed CP-MGM utilizes slightly more PMs but achieves a similar PM utilization ratio than the complementary CP-MGM. Moreover, the proposed CP-MGM achieves a reduction of PM consumption by 12% and an improvement of PM utilization ratio by 30%, when compared with the complementary SM-MGM.

TABLE 8. Power losses and efficiency of the three machines.

Items	MGM1	MGM2	MGM3
Iron loss (W)	79.79	115.43	130.35
Copper loss (W)	86.69	86.69	86.69
PM eddy current loss (W)	19.32	6.33	13.81
ICE input power (W)	1667	1711	1876
Efficiency (%)	88.85	87.82	87.69

MGM1: Complementary SM-MGM [27]; MGM2: Complementary CP-MGM; MGM3: The proposed CP-MGM.

D. EFFICIENCY

When the outer and inner rotors of an MGM are connected to the ICE crankshaft and wheels of an HEV, the MGM will work as a power split machine. In this case, part of the power from ICE (P_{ICE}) is transferred to the wheels as traction power (P_{tr}), while the rest of P_{ICE} is converted to electrical power (P_{e}) through stator winding.

Neglecting the mechanical loss, the power loss mainly consists of copper loss and iron loss. The efficiency of the power split machine is defined as

$$\eta_{PSD} = \frac{P_{tr} + P_e}{P_{ICE}} \times 100\% \tag{35}$$

When operating at rated condition, i.e., the inner and outer rotors rotate at 1200 r/min and 1600 r/min, respectively, with the stator current of 8.5 A (rms). The main losses and efficiency of the three machines are calculated by FEA and shown in Table 8. As can be seen, the proposed CP-MGM exhibits the highest iron loss due to abundant magnetic field harmonics and enhanced airgap flux density, caused by consequent-pole structure and axial magnetized PMs, respectively. In contrast, the iron loss of the complementary SM-MGM is the lowest, attributed to increased equivalent airgap length and reduced magnetic field harmonics contributed by surface-mounted structure. Besides, the copper losses of the three machines are the same owing to identical winding configuration and stator current. Moreover, the PM eddy current loss of the proposed CP-MGM is reduced, as compared with the complementary SM-MGM. This is due to the reduced PM consumption in the proposed CP-MGM. Taking these three types of losses into account, the efficiency of the proposed CP-MGM is 87.69%, which is slightly lower than that of the complementary SM-MGM and CP-MGM, i.e., 88.85% and 87.82%, respectively.

VI. CONCLUSION

This paper presents the design and optimization of a novel CP-MGM. Firstly, based on flux modulation theory, it is revealed that the asymmetrical magnetic circuit problem is a common issue for MGMs, which is attributed to the magnetic gearing effect and dual mechanical-port structure.

Therefore, a modular structure featuring enhanced harmonic elimination is proposed to solve the asymmetrical issue, achieved by artfully designed axially shifted angles. It is demonstrated that the majority of the non-working harmonics in the proposed design are eliminated, leading to a significant reduction in cogging torque and back EMF harmonics. Besides, the flux modulator width ratio and PM arc ratio are optimized to further improve the performance of the proposed CP-MGM, providing a general design guideline for CP-MGMs. Furthermore, the axially magnetized PMs are embedded in the flux barrier to further improve the output torque. 3D-FEA results show that the proposed CP-MGM can achieve symmetrical back EMF waveforms and significantly reduced torque ripple, as well as high torque density and high PM utilization ratio. The obtained knowledge from this paper will serve as the foundation in our future research and prototypes will be developed in our future papers.

REFERENCES

[1] J. Mei, C. H. T. Lee, and J. L. Kirtley, "Design of axial flux induction motor with reduced back iron for electric vehicles," *IEEE Trans. Veh. Technol.*, vol. 69, no. 1, pp. 293–301, Jan. 2020.
[2] K. T. Chau and C. C. Chan, "Emerging energy-efficient technologies for hybrid electric vehicles," *Proc. IEEE*, vol. 95, no. 4, pp. 821–835, Apr. 2007.
[3] X. Zhang, C.-T. Li, D. Kum, and H. Peng, "Prius$^+$ and Volt$^-$: Configuration analysis of power-split hybrid vehicles with a single planetary gear," *IEEE Trans. Veh. Technol.*, vol. 61, no. 8, pp. 3544–3552, Oct. 2012.
[4] J. M. Miller, "Hybrid electric vehicle propulsion system architectures of the e-CVT type," *IEEE Trans. Power Electron.*, vol. 21, no. 3, pp. 756–767, May 2006.
[5] C. Liu, K. T. Chau, C. H. T. Lee, and Z. Song, "A critical review of advanced electric machines and control strategies for electric vehicles," *Proc. IEEE*, early access, Dec. 10, 2020, doi: 10.1109/JPROC.2020.3041417.
[6] Q. Xu, F. Wang, X. Zhang, and S. Cui, "Research on the efficiency optimization control of the regenerative braking system of hybrid electrical vehicle based on electrical variable transmission," *IEEE Access*, vol. 7, pp. 116823–116834, 2019.
[7] S. Saponara, C. H. T. Lee, N. X. Wang, and J. L. Kirtley, "Electric drives and power chargers: Recent solutions to improve performance and energy efficiency for hybrid and fully electric vehicles," *IEEE Veh. Technol. Mag.*, vol. 15, no. 1, pp. 73–83, Mar. 2020.
[8] K. T. Chau, D. Zhang, J. Z. Jiang, C. Liu, and Y. Zhang, "Design of a magnetic-geared outer-rotor permanent-magnet brushless motor for electric vehicles," *IEEE Trans. Magn.*, vol. 43, no. 6, pp. 2504–2506, Jun. 2007.
[9] K. Atallah, J. Wang, S. D. Calverley, and S. Duggan, "Design and operation of a magnetic continuously variable transmission," *IEEE Trans. Ind. Appl.*, vol. 48, no. 4, pp. 1288–1295, Jul. 2012.
[10] S. Niu, S. L. Ho, and W. N. Fu, "Design of a novel electrical continuously variable transmission system based on harmonic spectra analysis of magnetic field," *IEEE Trans. Magn.*, vol. 49, no. 5, pp. 2161–2164, May 2013.
[11] S. Niu, T. Sheng, X. Zhao, and X. Zhang, "Operation principle and torque component quantification of short-pitched flux-bidirectional-modulation machine," *IEEE Access*, vol. 7, pp. 136676–136685, 2019.
[12] K. Atallah and D. Howe, "A novel high-performance magnetic gear," *IEEE Trans. Magn.*, vol. 37, no. 4, pp. 2844–2846, Jul. 2001.
[13] J. Bai, P. Zheng, C. Tong, Z. Song, and Q. Zhao, "Characteristic analysis and verification of the Magnetic-Field-Modulated brushless double-rotor machine," *IEEE Trans. Ind. Electron.*, vol. 62, no. 7, pp. 4023–4033, Jul. 2015.
[14] H. Chen and C. H. T. Lee, "Parametric sensitivity analysis and design optimization of an interior permanent magnet synchronous motor," *IEEE Access*, vol. 7, pp. 159918–159929, Nov. 2019.
[15] P. Chmelicek, S. D. Calverley, R. S. Dragan, and K. Atallah, "Dual rotor magnetically geared power split device for hybrid electric vehicles," *IEEE Trans. Ind. Appl.*, vol. 55, no. 2, pp. 1484–1494, Mar. 2019.
[16] J.-W. Kwon, N. Baloch, and B.-I. Kwon, "High gear ratio flux switching permanent magnet machine for high torque performance," *IEEE Access*, vol. 8, pp. 121630–121636, 2020.
[17] J. Bai, J. Liu, P. Zheng, and C. Tong, "Design and analysis of a magnetic-field modulated brushless double-rotor machine—Part II: Winding configuration," *IEEE Trans. Ind. Electron.*, vol. 66, no. 4, pp. 2550–2560, Apr. 2019.
[18] X. Ren, D. Li, R. Qu, and T. Pei, "Back EMF harmonic analysis of permanent magnet magnetic geared machine," *IEEE Trans. Ind. Electron.*, vol. 67, no. 8, pp. 6248–6258, Aug. 2020.
[19] X. Li, F. Shen, S. Yu, and Z. Xue, "Flux-regulation principle and performance analysis of a novel axial partitioned stator hybrid-excitation flux-switching machine using parallel magnetic circuit," *IEEE Trans. Ind. Electron.*, early access, Jun. 17, 2020, doi: 10.1109/.TIE.2020.3001807.
[20] A. Arif, N. Baloch, and B.-I. Kwon, "Winding switching and turn switching in permanent magnet Vernier machines for wide speed range operation and high efficiency," *IEEE Access*, vol. 7, pp. 55344–55357, 2019.
[21] L. Jing, Z. Huang, J. Chen, and R. Qu, "Design, analysis, and realization of a hybrid-excited magnetic gear during overload," *IEEE Trans. Ind. Appl.*, vol. 56, no. 5, pp. 4812–4819, Sep. 2020.
[22] Y. Wang, S. Niu, and W. Fu, "Electrical-continuously variable transmission system based on doubly fed flux-bidirectional modulation," *IEEE Trans. Ind. Electron.*, vol. 64, no. 4, pp. 2722–2731, Apr. 2017.
[23] Z. Q. Zhu, M. F. H. Khatab, H. Y. Li, and Y. Liu, "A novel axial flux magnetically geared machine for power split application," in *Proc. 12th Int. Conf. Ecol. Vehicles Renew. Energies (EVER)*, Apr. 2017, pp. 1–8.
[24] M. Wang, C. Tong, Z. Song, J. Liu, and P. Zheng, "Performance analysis of an axial magnetic-field-modulated brushless double-rotor machine for hybrid electric vehicles," *IEEE Trans. Ind. Electron.*, vol. 66, no. 1, pp. 806–817, Jan. 2019.
[25] M. Wang, P. Zheng, C. Tong, Q. Zhao, and G. Qiao, "Research on a transverse-flux brushless double-rotor machine for hybrid electric vehicles," *IEEE Trans. Ind. Electron.*, vol. 66, no. 2, pp. 1032–1043, Feb. 2019.
[26] K. Wang, F. Li, H. Y. Sun, and X. D. Sun, "Consequent pole permanent magnet machine with modular stator," *IEEE Trans. Veh. Technol.*, vol. 69, no. 7, pp. 7054–7063, Jul. 2020.
[27] L. Sun, M. Cheng, J. Zhang, and L. Song, "Analysis and control of complementary magnetic-geared dual-rotor motor," *IEEE Trans. Ind. Electron.*, vol. 63, no. 11, pp. 6715–6725, Nov. 2016.
[28] P. O. Rasmussen, T. O. Andersen, F. T. Jorgensen, and O. Nielsen, "Development of a high-performance magnetic gear," *IEEE Trans. Ind. Appl.*, vol. 41, no. 3, pp. 764–770, May 2005.
[29] L. Jing, J. Gong, Z. Huang, T. Ben, and Y. Huang, "A new structure for the magnetic gear," *IEEE Access*, vol. 7, pp. 75550–75555, 2019.
[30] J.-X. Shen, H.-Y. Li, H. Hao, and M.-J. Jin, "A coaxial magnetic gear with consequent-pole rotors," *IEEE Trans. Energy Convers.*, vol. 32, no. 1, pp. 267–275, Mar. 2017.
[31] M. Cheng, P. Han, and W. Hua, "General airgap field modulation theory for electrical machines," *IEEE Trans. Ind. Electron.*, vol. 64, no. 8, pp. 6063–6074, Aug. 2017.
[32] Z. Q. Zhu, D. Howe, E. Bolte, and B. Ackermann, "Instantaneous magnetic field distribution in brushless permanent magnet DC motors. I. Open-circuit field," *IEEE Trans. Magn.*, vol. 29, no. 1, pp. 124–135, Jan. 1993.

SHUANGCHUN XIE (Graduate Student Member, IEEE) received the B.Sc. degree in electrical engineering and automation from the Nanjing University of Aeronautics and Astronautics, Nanjing, China, in 2017. He is currently pursuing the Ph.D. degree with the School of Electrical and Electronic Engineering, Nanyang Technological University, Singapore. His research interests include power electronics, electrical machines and drives, and electric vehicle technologies.

HAO CHEN (Member, IEEE) received the B.Sc. degree in electrical engineering from the School of Electrical Engineering, Beijing Jiaotong University, Beijing, China, in 2012, and the Ph.D. degree in control science and engineering from the School of Automation, Beijing Institute of Technology, Beijing, in 2019.

From 2016 to 2018, he was a joint Ph.D. student with the Department of Electrical and Computer Engineering, Marquette University, Milwaukee, WI, USA. He is currently a Postdoctoral Research Fellow with the School of Electrical and Electronic Engineering, Nanyang Technological University, Singapore. His research interests include design and optimization of electric machines, power electronic drives, and motor control.

YUEFEI ZUO (Member, IEEE) received the B.Sc. and Ph.D. degrees in electrical engineering and automation from the Nanjing University of Aeronautics and Astronautics, Nanjing, China, in 2010 and 2016, respectively.

Since July 2016, he has been working as a Lecturer with Jiangsu University. He is currently a Postdoctoral Research Fellow with the School of Electrical and Electronic Engineering, Nanyang Technological University, Singapore. His research interests include power electronics, electric machines and drives, and advanced control strategies.

FAWEN SHEN (Graduate Student Member, IEEE) was born in Shandong, China, in 1994. He received the B.Sc. and M.E. degrees in electrical engineering from the China University of Petroleum (East China), Shandong, in 2016 and 2019, respectively. He is currently pursuing the Ph.D. degree with the School of Electrical and Electronic Engineering, Nanyang Technological University, Singapore. His research interests include design and analysis of permanent-magnet electrical machines and integrated-power-electronics motors.

BOON SIEW HAN received the B.Eng. degree in mechatronics from the University of Sydney, Australia, in 2003, and the M.Sc. degree in mechatronics from Nanyang Technological University (NTU), Singapore, in 2007. He is currently the Chief Information Officer at Schaeffler (Asia Pacific), the Head of Advanced Research and Innovation, and the Director of the Schaeffler Hub for Advanced Research at NTU (SHARE@NTU), Schaeffler (Singapore) Pte Ltd. His research interests include embedded solutions, robotics and autonomous systems, autonomous solution, and digitalization and AI.

CHI CUONG HOANG received the B.Eng. degree in electrical and electronic engineering from Nanyang Technological University, Singapore, in 2014. He is currently working as an Advanced Development Engineer at Schaeffler (Singapore) Pte Ltd. His research interests include power system control, electric motor control, and electric vehicle technologies.

CHRISTOPHER H. T. LEE (Senior Member, IEEE) received the B.Eng. (Hons.) and Ph.D. degrees in electrical engineering from the Department of Electrical and Electronic Engineering, The University of Hong Kong, Hong Kong, in 2009 and 2016, respectively.

He currently works as an Assistant Professor with Nanyang Technological University, Singapore, a Visiting Assistant Professor with the Massachusetts Institute of Technology, USA, and an Honorary Assistant Professor with The University of Hong Kong. His research interests include electric machines and drives, renewable energies, and electromechanical propulsion technologies. In these areas, he has published one book, three books chapters, and over 80 refereed articles.

Dr. Lee has received many awards, including NRF Fellowship, Nanyang Assistant Professorship, Li Ka Shing Prize (the best Ph.D. thesis prize), and Croucher Foundation Fellowship. He is an Editor of the IEEE TRANSACTIONS ON ENERGY CONVERSION and an Associate Editor of IEEE ACCESS and *IET Renewable Power Generation*.